The 15th International Symposium on Magnetic Bearings, August 3-6, 2016, Mojiko Hotel, Kitakyushu, Japan

ISMB15

Modelling and Control Design Simulations of Permanent Magnet Flux-Switching Linear Bearingless Motor

Rafal P. JASTRZEBSKI, Pekko JAATINEN, Olli PYRHÖNEN
Dept. of Electrical Engineering, Lappeenranta University of Technology, 53851 Lappeenranta, Finland
E-mail: Rafal.Jastrzebski@lut.fi, Pekko.Jaatinen@lut.fi, Olli.Pyrhonen@lut.fi

Abstract
For permanent magnet (PM) motor structures in rotating systems, it is typical to retain the magnets in the rotor. This constrains the rotor structure and limits applicability, e.g., for high-speed and high-temperature conditions. Flux-switching PM (FSPM) motors can overcome this limitation. Recently, the FSPM bearingless motors have been developed for special applications. The FSPM concept can be adapted to liner motors. For the linear motors, magnets or windings placed on the mover significantly decrease complexity and cost for longer distances. Still, to separate control of airgap and torque (thrust) two sets of windings or multiphase windings have been required for both rotating FSPM and linear PM machines. The linear FSPM bearingless motor solution, which integrates the magnets, winding structure and all the driving and control electronics on the mover is desired for many applications. However, because of electromagnetic unbalances the machine design is entangled with the control limitations and requirements. We reveal a modelling methodology for accurate derivation of bearingless machine dynamic and static force parameters as a function of airgap, control currents and track position in extended operational range. Model-based control simulations based on the accurate derived plant models determine the achievable machine performance and levitation limitations. The design and modelling methodology is general and can be applied to different PM bearingless motors. In the case study of linear FSPM bearingless motor the airgap control is possible in the equivalent to classical AMBs manner where it is independent from the thrust control.

Keywords : Linear flux-switching PM motor, Bearingless motor, Self-bearing drive, Magnetic levitation, Digital control, Linear actuator

1. Introduction

In recent years, the interests among electrical engineering community for the topologies where the rotor magnets are located in the stator and not rotor has been growing. Already in 1955, Rauch and Johnson (1955) on an example of single-phase machines have shown the principles of flux switching permanent magnet (FSPM) rotating machines. FSPM motors offer high power density, simple rotor construction (with magnets located in the stator) suitable for high temperature operation and low manufacturing costs (Rotevatn, 2009). Various geometries of FSPM machines have been proposed and tested (Chen and Zhu, 2010). Generally, for the machines with odd number of stator poles / even number of rotor poles, e.g. 5/6, 11/12, 13/12, the electromagnetic unbalance has been problematic. The typically selected and well-studied configurations include 12/10 and 12/14 configurations (Rotevatn, 2009), (Cao, et al., 2014). The linear FSPM (LFSPM) motors produce thrust force without need of conversion from rotational torque. The 12/14 LFSPM configuration offers higher torque with smaller ripple compared to 12/10 configuration (Chen and Zhu, 2010). In the case of LFSPM machines, two additional teeth at the mover ends balance the magnetic circuit. Otherwise, the operation of the classical LFSPM motor is the same as its rotational protagonist. The electromagnetic design of LFSPM motors is more challenging compared with the FSPM motors because of end effects and high relative thrust force ripple.

In the industrial applications, we can observe the continuing trend to develop more integrated, affordable and intelligent solutions. Bearingless motors offer both the motoring and magnetic levitation functionality using one actuator. This solution decreases component number, overall machine size and potentially offers robust control that features built

in monitoring and diagnostics. Gruber, et al. (2014) and Amrhein (2015) proposed 6-phase 12/10 FSPM bearingless rotating motor. In the machine, the additional phases are necessary for a levitation control. Similarly, to rotating machines the magnetic levitation functionality can be supplemented to the linear machines. Kim, et al. (2010) proposed levitated mover with two opposing armatures and PM array installed on the rail. Hwang, et al. (2014) developed opposite system with multiple winding modules installed along the track and the PMs located only in the mover. Hwang et al. (2014) studied a vector control for multi-phase transverse flux PM linear synchronous motor in order to control airgap and position without separate windings. These PM linear synchronous motors are attractive in many industrial applications such as machine tools, automation systems, transportation (propulsion) and levitation systems (Lee, et al., 2014), (Gieras, et al., 2012). However, they have inherent slot (cogging) and end effects, non-balanced phases, high saturation effects and significant force ripple dependent on track position. For minimum cost, both the coils and the PMs as well as electronics should be installed on the mover while the number of phases should be minimized. The use of one three-phase winding is possible but challenging because of coupling, nonlinear and end effects. Therefore, the design of bearingless linear PM machine has to combine the accurate modelling and control simulations to assess performance.

For bearingless machines, nonlinearities and coupling effects make modelling and control very challenging. Assessment of levitation performance requires a feasible control model. This work focuses on application of finite element method (FEM) and control modelling methodology for bearingless linear PM machines. First, the proper *dq*-reference frame current angles are determined. Second, the accurate fluxes, inductances and forces of case study 3-phase 12/14 LFSPM bearingless machine in moving *dq*-reference frame are calculated. The FEM obtained parameters vary with currents, airgap and track angle (position). Third, the results are used to construct the accurate simulation control models. Finally, exemplary levitation controllers of the test case machine are designed and tested in simulations for different operating conditions. The levitation performance and limitations of LFSPM bearingless motor that has both PMs and windings integrated on the mover are evaluated. The presented modelling methodology is general and applicable for wide range of bearingless motors.

2. Basic FEM analysis

The LFSPM motor has been analyzed using JMAG FEM software. The mechanical model of the machine is imported form SolidWorks. Motor construction data is exemplary and based on a conventional geometry as presented by Cao, et al. (2014). The summary of the most important parameters has been given in Table 1.

Table 1. Design specification of case study LFSPM bearingless motor with item names according to Cao et al. (2014).

Items	Parameter values	Items	Parameter values
PM material (NdFeB)	NMX-S34GH Hitachi Metals	Mover tooth wide	10.7 mm
Lamination steel type	Sura M270-35	Mover height	61.3 mm
Turns per slot per coil	360	Mover yoke height	8.2 mm
Rated speed	1 m/s	Magnet height	55 mm
Phase Resistance	10 Ohm	Magnet width	10.85 mm
Weight of the mover	500 kg	Rail tooth width	16.3 mm
Mover stack length	55 mm	Rail teeth yoke width	30.1 mm
Mover pole pitch	50.4 mm	Rail yoke height	10 mm
Rail pole pitch	46.4 mm	Nominal airgap	1.25 mm

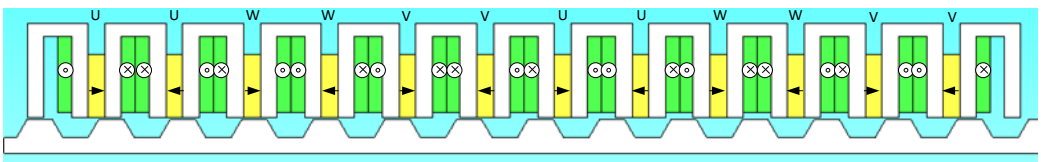

Fig. 1 Coil and magnet arrangement follows the 12-slot/14-pole structure of LFSPM motor, e.g. as in (Cao, et al., 2014), which is equivalent to rotating 12/14 configuration FSPM presented e.g., by Rotevatn (2009) but changed to the linear case. In all simulations 360° electrical corresponds to the rail pole pitch.

The assumed magnetic circuit, winding arrangements and magnetic pole structures are shown in Fig. 1.

Figure 2(a) shows that emf-voltage in one phase is slightly higher than in two other phases. This is due to effects of armature end tooth structure (end effect), which reduces emf-voltage in both *u* and *v*, phase, but not in *w* phase. The waveform is triangular because of strong magnetic saturation. The interaction between mover and rail poles creates cogging torque along the movement. The cogging force behavior in no-load situation is shown in Fig. 2(b). The net thrust force has about ±35 N. The net normal force of one motor seems almost constant along the movement due to high value. However, when mean value is subtracted the remaining ripple of net normal force is ±155 N. The cogging forces and end effects can be reduced (if required based on performance studies) e.g. by using rail pole skewing analogically to stator skewing (Jastrzebski, et al., 2015), introducing flux barriers (Cao, et al., 2014), (Jin, et al., 2009), shaping assistant teeth (Wang, et al., 2009), optimizing of rotor pole width (Zhu, et al., 2005) or changing motor slot/pole number.

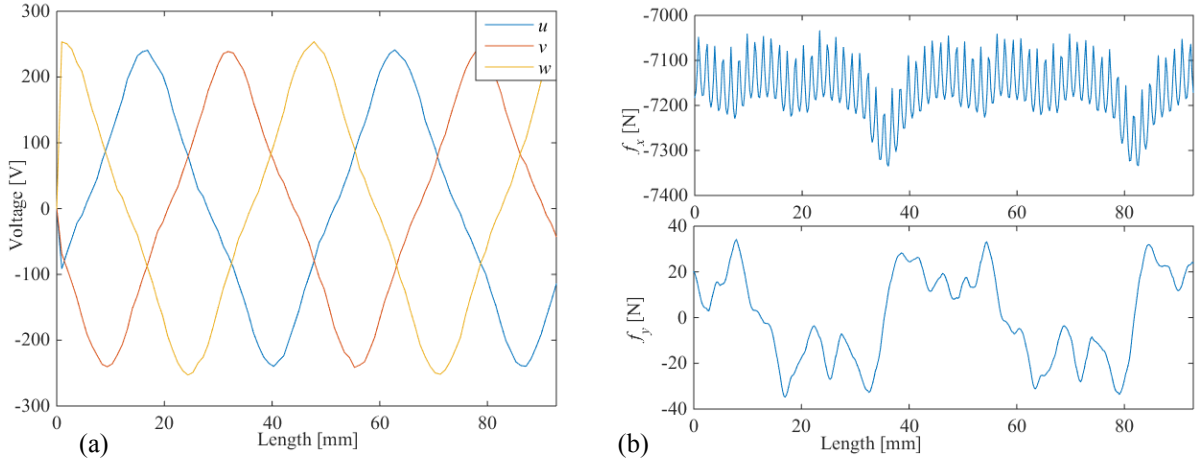

Fig. 2 (a) Back emf at no-load open circuit during movement of the armature to the left (according to Fig. 1) corresponding to two stator pole pitches. Symmetrical *u* and *v* (apart for the initial transient) but non-symmetrical *w* phase because of end effect. (b) Forces during no load back-emf test (moved for 720 deg).

3. Thrust and normal force analysis

The vector control of PM flux-switching machines requires definition of *d*- and *q*-axis for the system. For special machines, e.g. for odd number of slots and even number of poles or for complex winding arrangements these axes do not correspond to location of poles or magnets and are not immediately identifiable.

Here, we propose the method of determining the axes (or current vector positioning) of LFSPM motors based on FEM analysis of thrust and normal forces. We compute thrust and normal forces as functions of starting i_u phase current angle. Then, we record the mean values where initial transients are removed for better accuracy (Fig. 3(a)). Based on the mean values, we define the *d*-direction as corresponding to zero value of the thrust force. Alternatively, the assumed *d*-direction corresponds to the minimum value of the normal force (for opposite direction of *d*-axis). Based on performed simulations, such determined *dq*-axes are structure dependent and are the same regardless of the steel and magnet materials used.

After we define the axes, the magnetic forces of a single armature can be computed. When applying two opposite armatures as e.g. in (Jin, et al., 2009), the total thrust force is not significantly dependent on the airgap displacement of the mover. The thrust force is linearly dependent on the i_q current component at nominal and below values, as shown in Fig. 3(b). The nominal current is 3.6 Arms. The thrust force is fully independent of i_d current. This gives freedom to control the normal force by changing i_d currents, but no disturbance is created to the thrust force, since it is fully decoupled (in the studied operational region) from i_d by nature.

Bearingless operation of the linear machine requires controllable normal force. The normal force is mostly dependent on magnetizing current component i_d (Fig. 4(a)) but there is also coupling to force current component i_q when not in the nominal point (Fig. 4(b)). Both, the thrust force as well as the normal force saturate with high current amplitudes. The normal force variations are significant for very small airgaps. When opposite armatures have same i_q current and the air gap displacement from the middle point is zero, the normal forces of armatures cancel each other and the total normal force is independent on i_q current. Therefore, the opposite motor/armature transposition/shifting is not recommended as

a mean to reduce the thrust force ripple (It would introduce the normal force ripple).

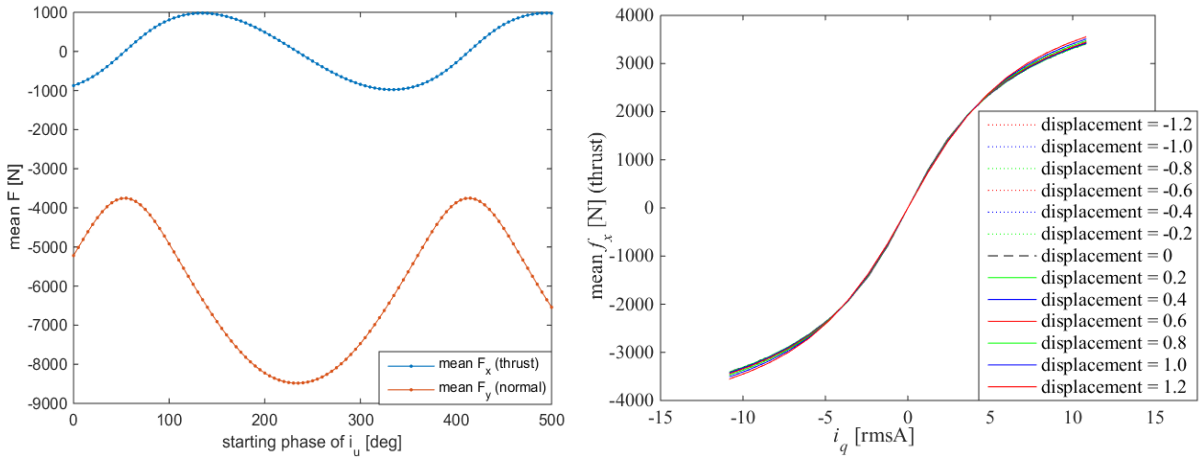

(a) (b)

Fig. 3 (a) Average forces as a function of starting i_u phase current angle. The current angel changes about 1.4 electrical period 500 deg. In this case, the maximum net thrust force angle is 143.4 deg and mean net normal force angle is 53.4 deg. These correspond to q- and d-axis angles for the current vector control of the machine. (b) Total thrust force of two opposite armatures as a function of i_q (i_d=0A) with different displacements from nominal airgap.

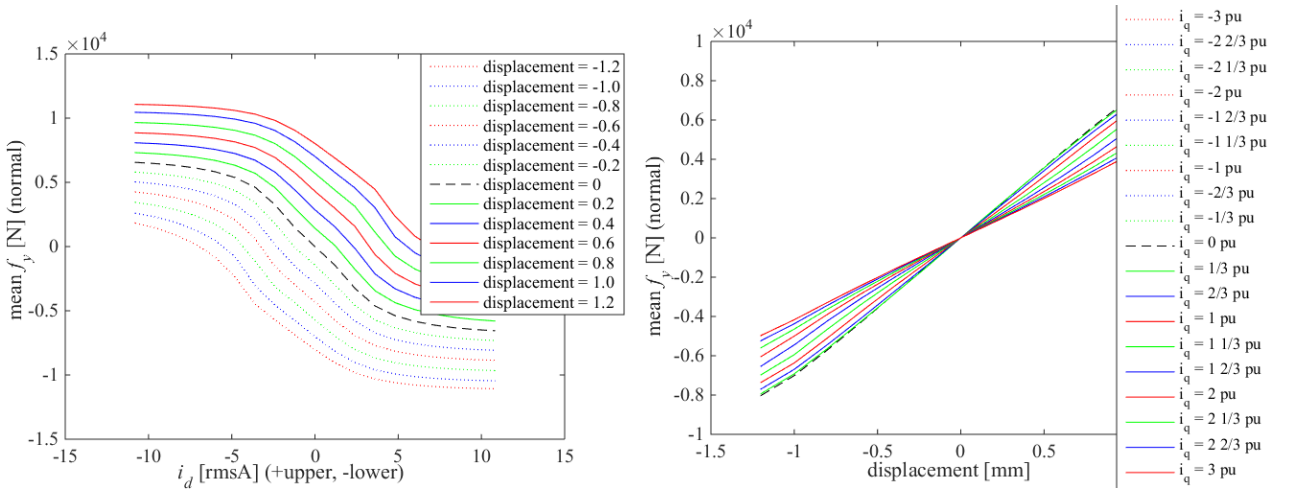

(a) (b)

Fig. 4 (a) Total normal force of two opposite armatures as a function of i_d current (i_q=0A) when i_d currents at opposite armatures are changed with opposite current values. (b) f_y as function of different displacements from nominal airgap for various i_q current (i_d=0A).

4. System modelling and control simulations

Analysis of levitation control requires dynamic modeling of the system. In the basic configuration, the 1DOF levitation and thrust are modelled as a point mass m. The force relations are linearized in the operational point using current stiffness k_{iqx}, k_{idy}, k_{iqy} and position stiffness k_y. For the thrust, the derivation of the PM flux linkage Ψ_{PM} is applied.

$$f_x = m\frac{d^2x}{dt^2},\ f_y = m\frac{d^2y}{dt^2}, \tag{1}$$

$$f_x = \frac{d\Psi_{\mathrm{PM}}}{dx}i_q = k_{iqx}i_q,\ f_y = k_y y + k_{idy}i_d + k_{iqy}i_q. \tag{2}$$

The forces and inductances used in the simulation model consist of 4-dimentional look-up tables computed in FEM for currents transformed to the moving dq-reference frame. Figure 5 shows the magnetic forces of a single armature. For

balancing magnetic pull, two opposing armatures are applied following e.g. Kim, et al. (2010) and Hwang, et al. (2014). Figure 6 shows L_d and L_q inductances and M_{dq} and M_{qd} mutual inductances averaged over different track angles. M_{qd} as well as the influence of the i_d current on f_q can be neglected in the linearized model. The dq-axes voltages are

$$v_d = Ri_d + L_d\frac{di_\mathrm{d}}{dt} + M_{dq}\frac{di_\mathrm{q}}{dt},\ v_q = Ri_q + L_q\frac{di_\mathrm{q}}{dt} + M_{qd}\frac{di_d}{dt}. \tag{3}$$

The inductances are computed as, e.g. $L_q = \left(\Phi_\mathrm{q}(x, i_q, y) - \Phi_\mathrm{q}(x, i_q = 0, y)\right)/i_q$, from the peak values of fluxes Φ and currents. The inductance values at i=0 are interpolated from other points. Alternative methods for computing machine inductances would be to use signal increments instead of peak values or to use first harmonic values after FFT of the signals. The accuracy of FFT is dependent on number of samples. An interesting alternative is to replace the inductance model with the flux model and derivatives in eq. (3). The fluxes and inductances vary considerably with the track angle. The model assumes some sensor delay (100 µs). The discretization time is 100 µs, which is typical for motor inverter current control loops. The linearized parameters at the nominal airgap are: k_{iqx}=650 N/Arms, $k_{idy,}$=-1217 N/Arms, $k_{iqy,}$=0 N/Arms, k_y=712000 N/m, L_d=0.32 H, L_q=0.43 H, M_{dq}=0 H, M_{qd}=0 H, R=8.5Ω. The sign and value of the mutual inductance M_{dq} depends on i_q. The position stiffness k_y also vary with i_q.

The initial step from one side to the middle point requires at least i_d =7 Arms current, which creates positive normal force (Fig. 4(a)), to move the mover to the zero airgap displacement position. In practice, the airgap can be limited reducing the current loading during the initial lift up. The simulation diagram is shown in Fig. 7 and the simulation results are shown in Fig. 8. The model-based linear quadratic Gaussian control and controller loop transfer recovery for the outer position controller synthesis are applied. The observer comprises estimation of inner current control loop, position control loop and augmented constant disturbance estimator. The inner current control is of P type.

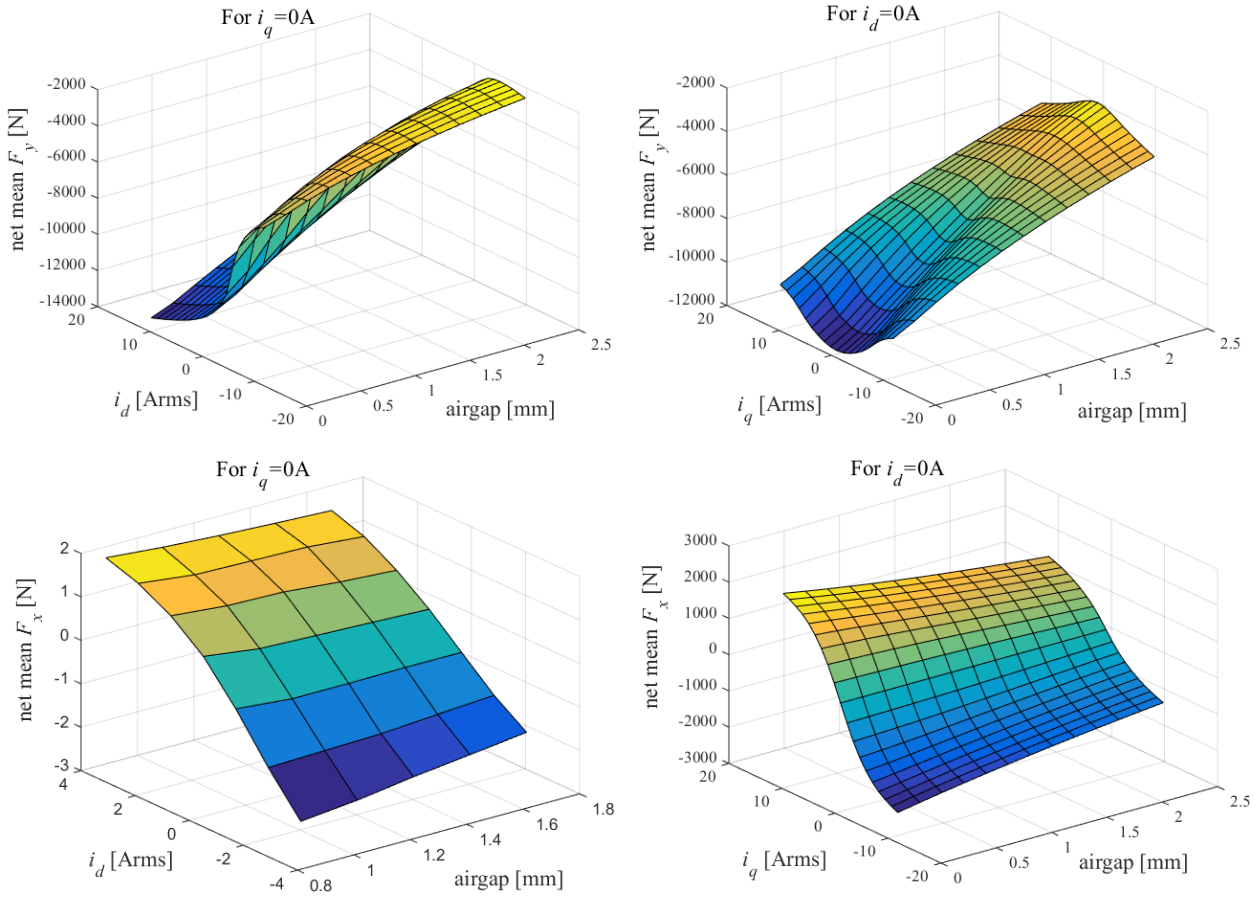

Fig. 5 Force characteristics of single armature averaged over different track angles as a function of current and the airgap in the operational range. Normal force dependent on i_d (a) and i_q (b). Thrust force dependent on i_d (c) and i_q (d).

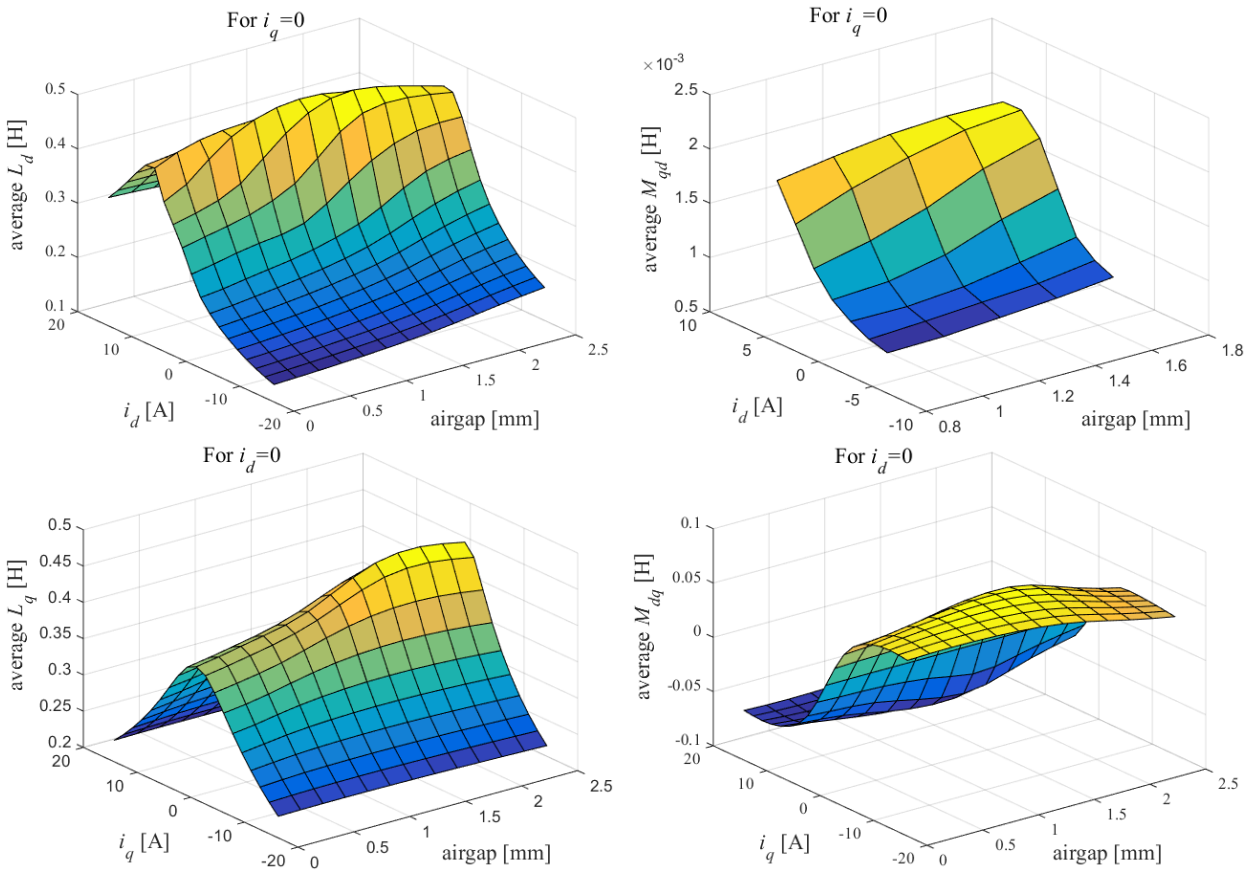

Fig. 6 Inductances and mutual inductances. There is some mutual inductance M_{dq} but not M_{qd}. Analogically, no influence of the *d*-current can be seen over thrust force.

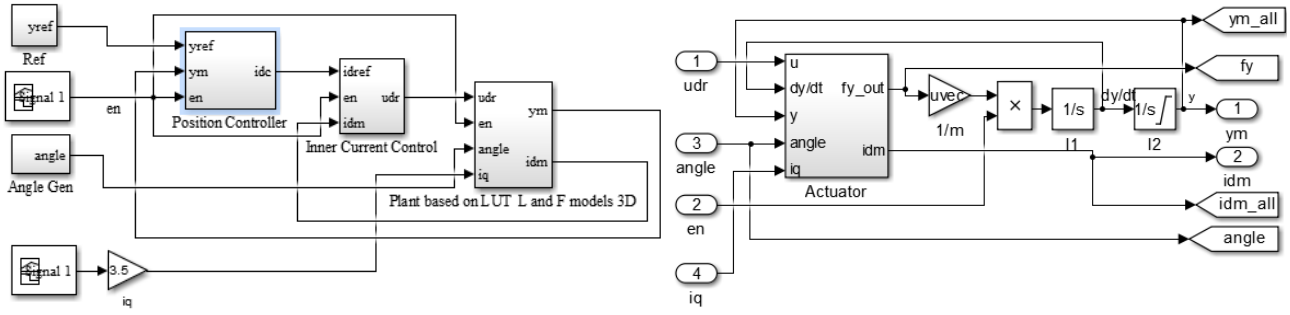

(a) Simulation top model with model based control. (b) Plant model with actuator based on 3D LUT models.

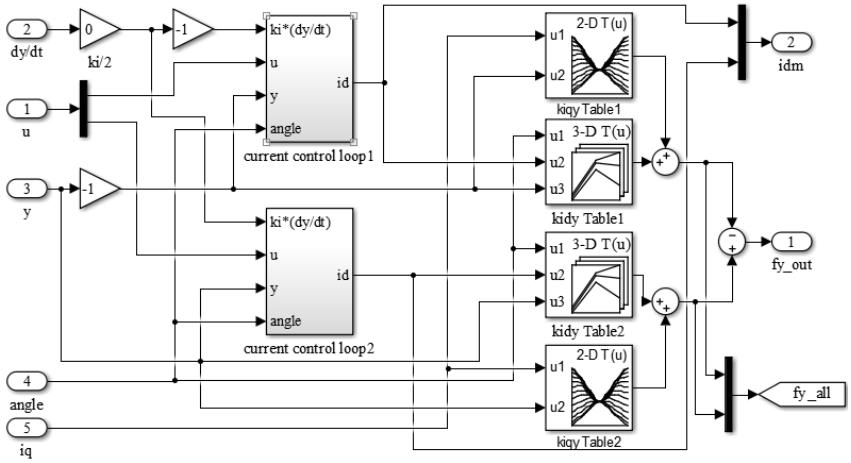

Fig. 7. (c) Actuator model with 2 current dynamical models.

In Figure 8 the coupling effects of thrust force and i_q current on normal force f_y can be observed. The track position has significant effect on the currents, positions and voltages. Potentially, it can excite some of the mechanical resonances of the real system. Therefore, the electromagnetic machine design should be updated to minimize the cogging effects.

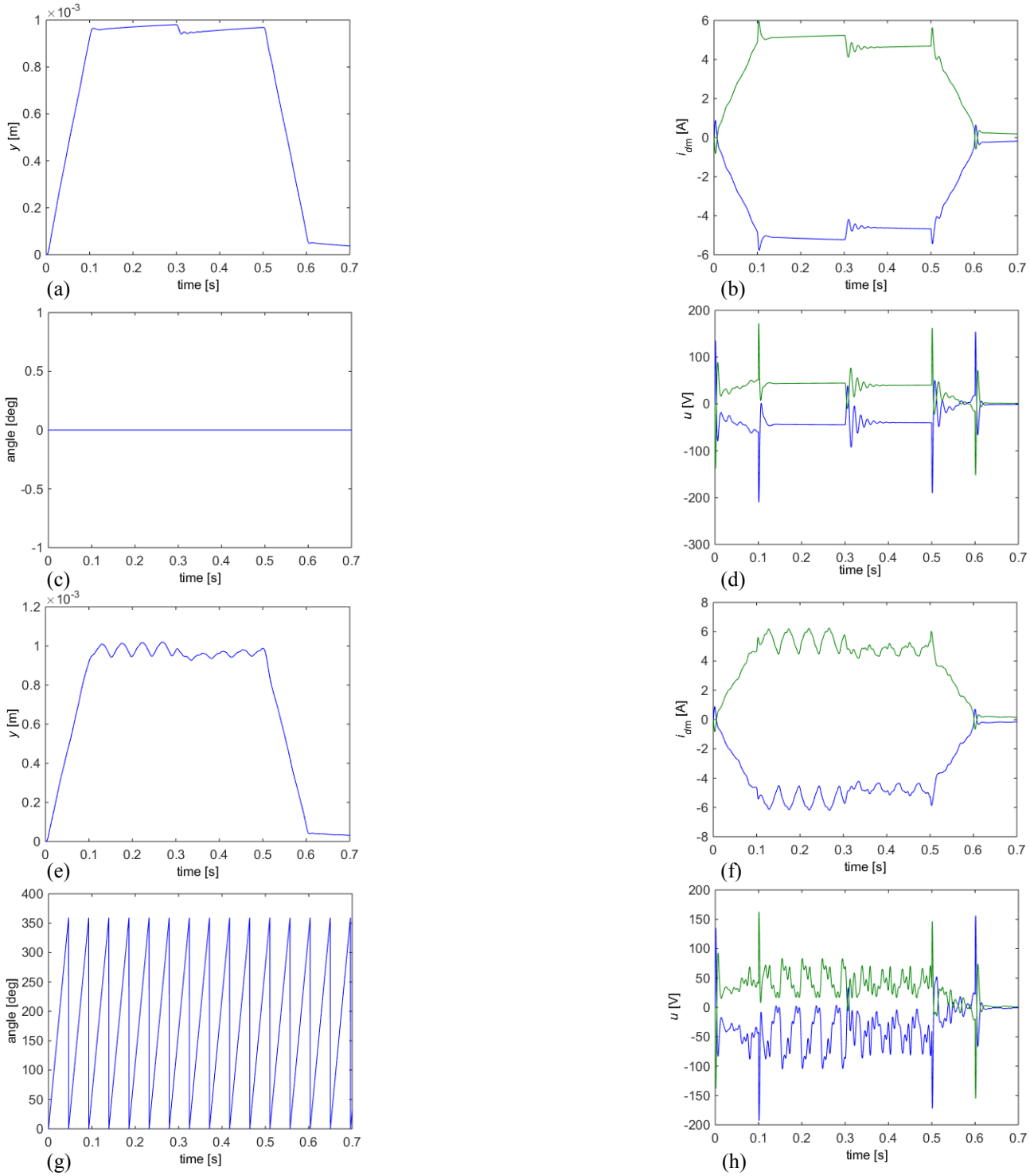

Fig. 8. Following a trapezoidal reference position y_{ref}. At t=0.3 s a 3.5 A step i_q current is applied. (a) y output for mover, which is not traveling in x direction. (b) i_d current. (c) Angle. (d) Voltage. (e) y output for mover, which is traveling with nominal speed in x direction. (f) i_d current. (g) Angle. (h) Voltage.

5. Conclusions

In the performed levitation control, the effects of inherent machine force ripple and quality of feedback on dynamical behavior of position control are studied. The model-based control provides stable and robust suspension. The system

arrangement has similar features compared to the levitation control in active magnetic bearing systems.

The mean normal force f_y resulting from the single armature is nonlinearly dependent on i and airgap y in the wider operational range. For two opposing armatures at no load the current stiffness and negative position stiffness are close to linear in normal operation range (for the current equal ± 4 Arms and for displacement from mid position ±0.5 mm). The normal force f_x ripple is below 3 % for i_d from 0 to 1pu and at no-load and at no airgap displacement. The coupling between the normal force and thrust force increases with increased airgap displacement.

The influence of the i_d current on the mean thrust force f_x can be neglected. However, the thrust force ripple (shape) for variable track position x depends on i_d. The influence of the airgap on the thrust force of the pair opposing armatures can be neglected in the normal operation range. The presented modelling and control design methodology led to successful evaluation of levitation performance of LFSPM machine.

Acknowledgment

The work has been co-funded by Academy of Finland No. 270012 and No. 273489.

References

Amrhein, W., Gruber, W., Bauer, W., and Reisinger, M., Magnetic Levitation Systems for Cost-Sensitive Applications, in Proc. of 2015 IEEE Workshop on In Electrical Machines Design, Control and Diagnosis (WEMDCD), (2015), pp. 104–111.

Cao, R., Cheng, M., Mi, C.C., and Hua, W., Influence of Leading Design Parameters on the Force Performance of a Complementary and Modular Linear Flux-Switching Permanent-Magnet Motor, IEEE Transactions on Industrial Electronics, Vol. 61, No. 5, (2014), pp. 2165–2175.

Chen, J. T., and Zhu, Z.Q., Comparison of all- and alternate-poles-wound flux-switching PM machines having different stator and rotor pole numbers, IEEE Transactions on Industry Applications, Vol. 46, No. 4, (2010), pp. 1406–1415.

Gieras, J.F., Piech, Z.J., Tomczuk, B.Z., Linear synchronous motors – Transportation and automation systems (2012), 2nd ed., CRC Press Taylor and Francis Group, p. 251–429.

Gruber, W., Radman, K., and Schob, R.T., Design of a Bearingless Flux-Switching Slice Motor Wolfgang, In Proc. of the 2014 International Power Electronics Conference Design, (2014), pp. 1691–1696.

Hwang, S.-H., Bang, D.-J. and Kim, J.-W., Air Gap Control of Multi-phase Transverse Flux Permanent Magnet Linear Synchronous Motor by using Independent Vector Control, in Proc. of Int. Power Electronics Conf., (2014), pp. 2427–2432.

Jastrzebski, R.P. Jaatinen, P. Sugimoto, Pyrhönen, O., Chiba, A., Design of a bearingless 100 kW electric motor for high-speed applications, in Proc. of International Conference on Electrical Machines and Systems, (2015), pp. 2008–2014.

Jin, M. J., Wang, C. F., Shen, J. X., and Xia, B., A modular permanent-magnet flux-switching linear machine with fault-tolerant capability, IEEE Transactions on Magnetics, Vol. 45, No. 8, (2009), pp. 3179–3186.

Kim, W.Y., Lee, J. M., and Kim, S. J., Rolling motion control of a levitated mover in a permanent-magnet-type bearingless linear motor, IEEE Transactions on Magnetics, Vol. 46, No. 6, (2010), pp. 2482–2485.

Lee, K., Baek, J., Kim, J., Ahn, M., Jung, T., and Lee, M., Design of Electromagnetic Levitation Linear Bearing for FPD Glass Delivery Applications, in Proc. of ISMB14, (2014), pp. 407–411.

Rauch, S. E., and Johnson, L. J., Design Principles of Flux-Switch Alternators, Transactions of the American Institute of Electrical Engineers. Part III: Power Apparatus and Systems, Vol. 74, No. 3, (1955), pp. 1261–1268.

Rotevatn, N., Design and testing of Flux Switched Permanent Magnet (FSPM) Machines (2009), MSc, Norwegian University of Science and Technology Department of Electrical Power Engineering.

Thomas, A., Zhu, Z. Q., Jewell, G. W., and Howe, D., Flux-switching PM brushless machines with alternative stator and rotor pole combinations, In Proc. of 2008 International Conference on Electrical Machines and Systems, (2008), pp. 2986–2991.

Wang, C.F., Shen, J.X., Wang, Y., Wang, L.L., and Jin, M.J., A new method for reduction of detent force in permanent magnet flux-switching linear motors, IEEE Transactions on Magnetics, Vol. 45, No. 6, (2009), pp. 2843–2846.

Zhu, Z. Q., Pang, Y., Howe, D., Iwasaki, S., Deodhar, R., and Pride, A., Analysis of electromagnetic performance of flux-switching permanent-magnet machines by nonlinear adaptive lumped parameter magnetic circuit model, IEEE Transactions on Magnetics, Vol. 41, No. 11, (2005), pp. 4277–4287.